

# Modeling Firn Density through Spatially Varying Smoothed Arrhenius Regression

Philip A. White <sup>\*1</sup>, Durban G. Keeler <sup>†2</sup>, Daniel Sheanshang<sup>‡1</sup>, and Summer  
Rupper <sup>§2</sup>

<sup>1</sup>Department of Statistics, Brigham Young University, USA

<sup>2</sup>Department of Geography, University of Utah, USA

September 16, 2022

## Abstract

Scientists use firn (compacted snow) density models as a function of depth to understand climate processes, evaluate water accumulation trends, and estimate glacier mass balances. Firn densification is a thermal reaction often modeled in discrete density-dependent stages, each governed by a reaction rate called an Arrhenius constant. Because firn density data are collected at depths rather than times, we infer Arrhenius rate constants from differential equation depth-density models. Arrhenius constants are commonly assumed to be constant over wide regions, but these models can poorly match observed densities, suggesting the need for site-specific models.

Our dataset consists of 14,844 density measurements from 57 firn cores drilled at 56 sites in West Antarctica, taken from four research expeditions. For these data, we present a novel physically constrained spatially varying Arrhenius regression model for

---

\*Corresponding Author: pwhite@stat.byu.edu

†durban.keeler@gmail.com

‡danielsheanshang@gmail.com

§summer.rupper@geog.utah.edu

firn density as a function of depth. Because the Arrhenius regression framework is piecewise linear, we present a smoothed Arrhenius model that allows nonlinear deviations to better fit the data while preserving inference on physical parameters. Lastly, we use a unique hierarchical, heteroscedastic error model that accounts for differences between research expeditions. Using this model, we explore firn densification patterns change over space and compare our model to previous studies.

KEYWORDS: Arrhenius equation, Bayesian statistics, Gaussian process, spatial statistics

## 1 Introduction

We define Arrhenius regression to be a regression model where the regression slope (the Arrhenius rate constant) is specified by two physical constants, one of which relates temperature to reaction rate using first-order kinetics. To identify both physical constants in the Arrhenius rate constant, repeated reactions at different temperatures is necessary. A simple example of this would be determining the rate of a chemical reaction by measuring concentrations over time. In many scientific settings, including our motivating example, reaction rates can change over various stages of the reaction; thus, piecewise Arrhenius regression models are appropriate.

In our motivating problem, we observe firn (compacted snow) density measurements as a function of depth taken from 57 firn cores drilled at 56 sites over West Antarctica. From these data, we wish to infer densification rates over depth.

Models for Antarctic firn (snow) density estimation are essential to accurately determine the age-depth scale of the Antarctic ice sheets (Herron & Langway, 1980; Hörhold et al., 2011) which allows scientists to use drilled firn cores to track snow water accumulation over the recent past (Keeler et al., 2020). Moreover, understanding total mass loss in Antarctica is a primary research target within the scientific community, with critical implications for current and future sea-level rise (IPCC, 2013). A common approach for estimating total mass changes uses laser altimetry to measure elevation changes in the ice sheet and translates elevation changes into mass differences using firn density estimates (Li & Zwally, 2011). Importantly, no current remote sensing techniques permit the estimation of firn density, necessitating

reliance on in-situ measurements. Due to the remoteness and extreme environments of Antarctica, such measurements are costly to obtain, making improved utilization of existing data of paramount concern (Eisen et al., 2008). Altogether, understanding snow density processes in Antarctica is essential for evaluating the health of the earth’s largest freshwater reservoir.

Firn densification is a thermal reaction, and densification patterns change at various *critical densities* due to the interplay of particle rearrangement and plasticity change (Gow, 1975; Herron & Langway, 1980; Maeno & Ebinuma, 1983; Martinerie et al., 1992; Salamatin et al., 2009). Densification models often use three critical densities (Hörhold et al., 2011), giving a piecewise Arrhenius regression model with four stages, each with an Arrhenius constant. In this manuscript, we focus on variations of an example of an Arrhenius regression model presented in Herron & Langway (1980), where the reaction rates are not directly observed but are inferred from density changes over depth.

Although frequently assumed to be constant over spatial domains (Herron & Langway, 1980; Hörhold et al., 2011), the physics related to thermal reaction rates and critical densities depend on snow/firn type and conditions which change spatially (Alley et al., 1982; Johnson, 1998; Freitag et al., 2004). Therefore, Arrhenius constants and critical densities are not constant over space, something discussed by Hörhold et al. (2011) and in Section 2. Despite these findings, many current models rely on simple global fitting constraints averaged across all sites, often spanning both poles (Herron & Langway, 1980; Helsen et al., 2008; Arthern et al., 2010; Verjans et al., 2020). Capturing the spatial variation in these parameters would therefore improve the accuracy and general applicability of firn density models to more widespread regions.

Arrhenius rate constants are strictly positive, and reasonable values for critical densities are bounded. Snow density is bounded above by the density of ice  $\rho_I = 0.917 \text{ g/cm}^3$ , and, in general, snow density increases as a function of depth until it approaches the density of ice. Thus, appropriately constraining model parameters is essential.

Here, our goal is to understand how the physical properties of densification vary over West Antarctica. To meet this goal, we contribute a novel constrained, multivariate spatial model motivated by the physics of densification (See Section 2.1) and data attributes

discussed in Section 2. This model resolves the piecewise Arrhenius regression model’s identifiability issues through multivariate spatial smoothing or information sharing. To capture the appropriate constraints, we specify a multivariate Gaussian process model in the transformed parameters space and constrain the mean between 0 and  $\rho_I$ . From an inferential perspective, our spatial model allows us to spatially interpolate physical quantities, whose spatial properties are currently poorly understood.

Disadvantageously, the piecewise Arrhenius regression model is piecewise-linear and thus misses important nonlinear features of the snow density core. To remedy this and to improve prediction, we include a spatially-correlated smooth functional adjustment for each core. Because models of this type can often alter the interpretation of fixed effects (Hodges & Reich, 2010), Arrhenius constants in our setting, we constrain this smooth model to lie in the orthogonal column space of our physical model.

Our second set of contributions relates to accounting for differences in data acquisition. Different research groups drilled the firn cores and did not necessarily use the same approaches. Researchers acquire density measurements by taking volume and mass measurements over a length of the core that is not constant between field campaigns and is not always consistent for cores within the same field campaign. In general, if density measurements are taken from longer core segments, then the resulting snow density curve appears smoother. Most density measurements were taken in the field, which, unsurprisingly, poses several challenges. Many of the cores display anomalous density measurements that are likely erroneous, motivating the use of error distributions that down-weight these anomalies. Our error model accounts for heavy-tailed errors, research group effects, and possible weighting that accounts for differences in the core length used to measure firn density.

The proposed model provides important contributions to the polar and ice sheet research communities. Perhaps most importantly, the model performs spatial modeling of Arrhenius constants, allowing for improved prediction of depth-density curves based on regional differences across West Antarctica. This modeling also includes flexibility in the density/depth cutoffs between different stages of densification, better capturing the true variability in such parameters. The model also allows for non-linear deviations in densification rate parameters and is thus able to better handle noisy data, either from measurement errors or physical dis-

equilibrium effects. Finally, our model includes quantitative bounds of estimate uncertainty, both valuable attributes for cryospheric research. Most current observation-based firn density models include few if any of the above points. The proposed model therefore represents an important step forward in providing spatially-distributed and error-constrained estimates of density with depth in Antarctic firn from *in-situ* data.

We continue by discussing the firn densification processes and our firn density dataset in Section 2. In Section 3, we present the constrained spatial modeling framework based on the physics and data attributes discussed in Section 2. In Section 4, we give our model comparison approach (Section 4.1), our final model (Section 4.2), as well as prior distributions, model fitting and prediction Section 4.3). Based on our final model, we present results in Section 5.

## 2 Firn Densification Processes and Data

### 2.1 The Physics of Firn Densification

The Arrhenius constant is the rate of thermally driven reactions and is defined as

$$k = Ae^{-\frac{E}{RT}}, \quad (1)$$

where  $T$  is the temperature (in Kelvin),  $R \approx 8.314\text{JK}^{-1}\text{mol}^{-1}$  is the ideal gas constant,  $E > 0$  is the energy of activation, and  $A > 0$  is a pre-exponentiation factor. Because firn densification is thermally-activated, firn densification models rely on Arrhenius constants. For a single firn core with many snow density estimates, the Arrhenius constant  $k$  is statistically identifiable, but parameters  $A$  and  $E$  are not. However, many cores with different temperatures are needed to identify  $A$  and  $E$ , a process that could be carried out regionally to account for geographic differences. Firn densification models also rely on surface mass balance (SMB), the average rate of snow accumulation. Snow/ice density models as functions of depth generally use the thermal physics of densification (Cuffey & Paterson, 2010), empirical fits to data using exponential functions (Miège et al., 2013), or a combination of the two (Herron & Langway, 1980; Hörhold et al., 2011).

We focus our modeling discussion on the hybrid model proposed by [Herron & Langway \(1980\)](#), an example of a piecewise Arrhenius regression model frequently used in polar research. Henceforth, we call this the HL model. The HL model is a model for density as a function of depth and notably excludes time. The HL model, however, is derived using firn densification rate models, and, for this reason, the HL model can be used for core aging ([Herron & Langway, 1980](#)).

The HL model is defined in stages, where the behavior of the model changes at critical densities where various physical forces alter the pattern of densification (see [Hörhold et al., 2011](#), for review and discussion). The HL model defines rates of densification using Arrhenius constants for two stages: for densities less than 0.55 g/cm<sup>3</sup> and between 0.55 g/cm<sup>3</sup> and 0.80 g/cm<sup>3</sup>. The model is

$$\begin{aligned} \rho_I k_1 x + \log \left( \frac{y(0)}{\rho_I - y(0)} \right), & \quad \text{for } x \in [0, \kappa_1), \\ \frac{\rho_I k_2 (x - \kappa_1)}{\sqrt{SMB}} + \log \left( \frac{y(\kappa_1)}{\rho_I - y(\kappa_1)} \right), & \quad \text{for } x \in [\kappa_1, \kappa_2), \end{aligned} \quad (2)$$

where  $k_1 = 11 \exp \{-10160/RT\}$ ,  $k_2 = 575 \exp \{-21400/RT\}$ , and  $T$  is the temperature 10-m below the surface.

Depths  $\kappa_1$  and  $\kappa_2$  corresponding to the densities 0.55 and 0.80 can be extracted from (2) as

$$\begin{aligned} \kappa_1 &= \frac{1}{\rho_I k_1} \left[ \log \left( \frac{0.55}{\rho_I - 0.55} \right) - \log \left( \frac{y(0)}{\rho_I - y(0)} \right) \right], \\ \kappa_2 &= \kappa_1 + \frac{\sqrt{SMB}}{\rho_I k_2} \left[ \log \left( \frac{0.80}{\rho_I - 0.80} \right) - \log \left( \frac{0.55}{\rho_I - 0.55} \right) \right]. \end{aligned} \quad (3)$$

When comparing the HL model to field data, [Hörhold et al. \(2011\)](#) find good agreement to data at some sites and poor agreement at other sites. Fitting site-specific HL models, we observe similar issues for our data. Moreover, we find spatial patterns in the surface densities and the Arrhenius constants, as we discuss in Section 2. For these reasons, we propose spatially-varying versions of (2) in Section 3.

More recent models often assume that there are three critical densities at 0.55, 0.73, and between 0.82 – 0.84 g/cm<sup>3</sup> (see [Hörhold et al., 2011](#), for review and discussion), which we call  $\rho_1$ ,  $\rho_2$ , and  $\rho_3$ . For each critical density,  $\rho_1$ ,  $\rho_2$ , and  $\rho_3$ , there is a corresponding critical

depth  $\kappa_1$ ,  $\kappa_2$ , and  $\kappa_3$ . Using high-resolution density measurements, [Hörhold et al. \(2011\)](#) find that the first critical density  $\rho_1$  ranged between 0.45 and 0.60 g/cm<sup>3</sup>, rather than at 0.55 g/cm<sup>3</sup>, depending on the site. Moreover, [Hörhold et al. \(2011\)](#) argue that the density transitions at critical densities  $\rho_2$  and  $\rho_3$  are only “weakly apparent.” Because of this, we set the hierarchical mean for these stages to be the same, but parameters may differ site-to-site.

Rather than a two-stage model, we suggest a four-stage model that incorporates more recent extensions of the HL model with three random critical densities  $\rho_1$ ,  $\rho_2$ , and  $\rho_3$ . As discussed, because the transitions at  $\rho_2$  and  $\rho_3$  are weak, we assume that the hierarchical mean parameters for the second, third, and fourth stages are equal, but we do not constrain the site-specific parameters to be equal.

We connect the physical and statistical models by writing the four-stage version of [\(2\)](#) as a generalized piecewise linear multiple regression model. Let  $\alpha$  be an intercept,  $\mathbf{z}(x)$  be depth-specific covariates with corresponding Arrhenius constants  $\mathbf{k}$ , and  $\mathbf{1}(\cdot)$  be an indicator function. The model can be written as

$$\begin{aligned} \log\left(\frac{y(x)}{\rho_I - y(x)}\right) &= \alpha + \mathbf{z}(x)^T \mathbf{k}, & \alpha &= \log\left(\frac{y(0)}{\rho_I - y(0)}\right) \\ z_1(x) &= \rho_I \min(x, \kappa_1), & z_3(x) &= \frac{\rho_I \min(x - \kappa_2, \kappa_3 - \kappa_2)}{\sqrt{SMB}} \mathbf{1}(x > \kappa_2), \\ z_2(x) &= \frac{\rho_I \min(x - \kappa_1, \kappa_2 - \kappa_1)}{\sqrt{SMB}} \mathbf{1}(x > \kappa_1), & z_4(x) &= \frac{\rho_I (x - \kappa_3)}{\sqrt{SMB}} \mathbf{1}(x > \kappa_3). \end{aligned} \tag{4}$$

In [Section 4.2](#), we present the hierarchical spatial model corresponding to [\(4\)](#).

## 2.2 Data

This dataset consists of  $N = 14,844$  density measurements from 57 firn/ice cores at  $n_s = 56$  unique locations. These data come from four different field campaigns: the East Antarctic Plateau ([Albert et al., 2004](#)), the Siple Dome project ([Lamorey & Cooper, 2002](#)), the Satellite Era Accumulation Traverse ([Burgener et al., 2013](#)), and the US portion of the International Trans-Antarctic Scientific Expedition ([Mayewski et al., 2005](#)). We refer to these field campaigns as EAP, SDM, SEAT, and US, respectively.

We denote density measurements as  $y(\mathbf{s}_{ij}, x) > 0$  and the drilled core as  $\mathbf{s}_{ij}$ , where  $\mathbf{s}_i$

indicates the observed core location,  $j$  indexes replicates at the same site, and  $x$  represents depth. We let  $\mathcal{S}$  denote the collection of the 56 core sites  $\mathbf{s}_i$ . Because we use our model to estimate parameters where we do not have data, we let  $\mathbf{s}$  represent a generic spatial location. To specify campaign-specific parameters, we define  $m(\mathbf{s}_{ij})$  to be an indicator for which field campaign acquired core  $\mathbf{s}_{ij}$ .

The precise methods and techniques of density measurement are generally similar but differ somewhat across campaigns. Density measurements involve measuring the mass and volume of sections of a core. Density measurements are averaged over some length of the firn core; therefore, density variability relies not only on the mass and volume measurements themselves but also on the length of the core section used. We let  $dx_{\mathbf{s}_{ij}}$  be the length of the core used to procure a density measurement for core  $\mathbf{s}_{ij}$  (i.e., the maximum depth of that core divided by the number of density measurements). As discussed, we expect smoother snow density curves with longer  $dx_{\mathbf{s}_{ij}}$ . The core lengths for the EAP and SEAT campaigns are internally consistent in that, if  $m(\mathbf{s}_{ij}) = m(\mathbf{s}'_{ij'})$ ,  $dx_{\mathbf{s}_{ij}} = dx_{\mathbf{s}'_{ij'}}$ . The SDM and US expeditions do not use the same core lengths  $dx_{\mathbf{s}_{ij}}$  to measure density for each core, an issue we address through a heteroscedastic model.

In Figure 1, we plot the locations of the cores, the number of density measurements from each core, maximum depth of the core, and the observed density measurements as a function of depth for each site. Although snow density cannot exceed  $\rho_I$ , some measurements violate this limit, suggesting that our model for  $y(\mathbf{s}_{ij}, x)$  must permit values greater than  $\rho_I$ , while a reasonable model for the mean function should constrain it between  $(0, \rho_I]$ .

The HL model uses SMB and the average temperature 10-m below the surface ( $T(\mathbf{s})$ ). We have access to a dataset of temperature 10-m below the surface (Bohlander & Scambos, 2001) and the ERA-Interim 2-m air temperature data averaged from 1979 to 2014 (Molteni et al., 1996), which we call  $T_{(2)}(\mathbf{s})$  to distinguish it from  $T(\mathbf{s})$ . Because the ERA-Interim 2-m air temperature data is very coarse, we use a smoothed temperature surface (White et al., 2019). In Figure 2, we plot the 2-m air temperature, observed temperature 10-m below the surface, and a scatterplot of these temperatures with a least-square regression line.

The average 2-m air temperature is higher than the temperature below the surface, and the relationship between the two temperatures appears to be linear with some heteroscedas-



ticity. The simple linear regression model has an  $R^2 = 0.923$ . Although there is relatively little variability in temperature 10-m below not explained by 2-m air temperature, there is also spatial autocorrelation in the residuals for temperature 10-m below the surface given 2-m air temperature. Thus, we use a simple spatially-varying intercept model to estimate  $T(\mathbf{s})$  at the 56 unique core locations and use the posterior mean of this model for the HL model. We use the posterior mean SMB from [White et al. \(2019\)](#) who use a spatial generalized linear model to interpolate  $SMB(\mathbf{s})$ . The posterior means of  $T(\mathbf{s})$  and  $SMB(\mathbf{s})$  are plotted in [Figure 2](#). While we could model density, temperature, and SMB jointly, joint modeling poses significant computational challenges.

Using the posterior means for  $T(\mathbf{s})$  and  $SMB(\mathbf{s})$  from [Figure 2](#), we compare the HL model to each core field data. While the model matches the overall trend of density in general, it fails to accurately estimate firn density in many cases. To illustrate, we plot the fit of the HL model for two SDM cores (cores 4 and 8), one SEAT core (core 13), and one US cores (core 49) in [Figure 3](#). The HL model fit to core 4 is generally good, undershoots the observed values for core 8, overshoots density measurements for much of core 12, and under- and over-estimates densities in core 49. These model failures suggest that a single HL model for all cores is inappropriate and that the model should vary site-to-site. We revisit the fits of our proposed models for these same cores in [Section 4.3](#).

We fit piecewise linear models with the same discontinuities as the HL model to explore whether we can leverage spatial patterns in model fits for our model. We fit these models on the logit-transformed density measurements less than  $\rho_I$  at each core. For each coefficient, we plot the binned semivariogram with the fit for an exponential semivariogram in [Figure 4](#) to explore spatial patterns in the estimated regression coefficients. These show clear spatial patterns motivating a spatial model for the parameters of the Arrhenius regression model.

### 3 Spatially-Varying Arrhenius Regression Models

#### 3.1 Spatially-Varying Arrhenius Regression Model

Motivated by the systematic errors in the HL model (Figure 3) and the spatial autocorrelation of parameters in Figure 4, we propose a joint hierarchical spatial model for the Arrhenius regression parameters for each stage of our model and the critical densities  $\rho_1$ ,  $\rho_2$ , and  $\rho_3$ . In this model, we denote the spatially-varying parameters for each stage of our model, indexed with the subscript  $l = 1, 2, 3, 4$ , as  $A_l(\mathbf{s})$ ,  $E_l(\mathbf{s})$ ,  $\rho_1(\mathbf{s})$ ,  $\rho_2(\mathbf{s})$ , and  $\rho_3(\mathbf{s})$ , respectively.

In this model, we specify a joint spatial process for parameters  $\alpha(\mathbf{s})$ ,  $A_l(\mathbf{s})$ ,  $E_l(\mathbf{s})$ ,  $\rho_1(\mathbf{s})$ ,  $\rho_2(\mathbf{s})$ , and  $\rho_3(\mathbf{s})$ . We model  $\alpha(\mathbf{s})$  using a Gaussian (spatial) process. Because  $A_l(\mathbf{s})$  and  $E_l(\mathbf{s})$  are positive, we model these parameters on the log scale. Similarly, we use transformations of  $\rho_1(\mathbf{s})$ ,  $\rho_2(\mathbf{s})$ , and  $\rho_3(\mathbf{s})$ . The spatially-varying Arrhenius model allows us to estimate how thermal processes vary over space. Moreover, because each stage of our model only has one rate, to make  $A_l(\mathbf{s})$  and  $E_l(\mathbf{s})$  identifiable, we use a spatial prior distribution that enables information sharing between sites.

Since firm density is bounded between  $(0, \rho_I]$ , we specify our mean function  $\mu(\mathbf{s}, x)$  as an HL model with spatially-varying components. We write this as

$$\log \left( \frac{\mu(\mathbf{s}, x)}{\rho_I - \mu(\mathbf{s}, x)} \right) = \alpha(\mathbf{s}) + \mathbf{z}_\theta(\mathbf{s}, x)^T \mathbf{k}(\mathbf{s}), \quad (5)$$

where  $\mathbf{z}_\theta(\mathbf{s}, x)$  and  $\mathbf{k}(\mathbf{s})$  are made up of elements

$$\begin{aligned} z_1(\mathbf{s}, x) &= \rho_I \min(x, \kappa_1(\mathbf{s})), & k_1(\mathbf{s}) &= A_1(\mathbf{s}) \exp \left( -\frac{E_1(\mathbf{s})}{RT(\mathbf{s})} \right) \\ z_2(\mathbf{s}, x) &= \frac{\rho_I \min(x - \kappa_1(\mathbf{s}), \kappa_2(\mathbf{s}) - \kappa_1(\mathbf{s}))}{\sqrt{SMB(\mathbf{s})}} \mathbf{1}(x > \kappa_1(\mathbf{s})), & k_2(\mathbf{s}) &= A_2(\mathbf{s}) \exp \left( -\frac{E_2(\mathbf{s})}{RT(\mathbf{s})} \right) \\ z_3(\mathbf{s}, x) &= \frac{\rho_I \min(x - \kappa_2(\mathbf{s}), \kappa_3(\mathbf{s}) - \kappa_2(\mathbf{s}))}{\sqrt{SMB(\mathbf{s})}} \mathbf{1}(x > \kappa_2(\mathbf{s})), & k_3(\mathbf{s}) &= A_3(\mathbf{s}) \exp \left( -\frac{E_3(\mathbf{s})}{RT(\mathbf{s})} \right) \\ z_4(\mathbf{s}, x) &= \frac{\rho_I (x - \kappa_3(\mathbf{s}))}{\sqrt{SMB(\mathbf{s})}} \mathbf{1}(x > \kappa_3(\mathbf{s})). & k_4(\mathbf{s}) &= A_4(\mathbf{s}) \exp \left( -\frac{E_4(\mathbf{s})}{RT(\mathbf{s})} \right) \end{aligned}$$

Because they are parameter dependent, we write the space-depth covariates as  $\mathbf{z}_\theta(\mathbf{s}, x)$ . Although we do not model the depth change points  $\kappa_1(\mathbf{s})$ ,  $\kappa_2(\mathbf{s})$ , and  $\kappa_3(\mathbf{s})$  directly, we infer

them from the critical densities  $\rho_1(\mathbf{s})$ ,  $\rho_2(\mathbf{s})$ , and  $\rho_3(\mathbf{s})$ , as in (3).

Somewhat as an aside, the model is a generalized linear I-spline model with unknown knots, where the critical depths  $\kappa_1(\mathbf{s})$ ,  $\kappa_2(\mathbf{s})$ , and  $\kappa_3(\mathbf{s})$  are equivalent to interior knots of the I-spline. I-splines are defined as the integral of M-spline, or, equivalently, as the integral of a scaled B-spline (see Ramsay, 1988; Meyer, 2008, for more details). White et al. (2020) use these for spatial modeling of monotone functions.

### 3.2 Smoothed Arrhenius Regression Model

Because the Arrhenius regression model is piecewise linear (on the transformed scale) and could thus miss important deviations from linearity, we present the *smoothed* Arrhenius regression model. Because Arrhenius parameter inference is essential, we constrain the smooth component of our model to lie in the orthogonal columns space of  $\mathbf{z}_\theta(\mathbf{s}, x)$  for each core. If parameter inference is the only goal of the model, then this extension may be unnecessary. However, with a dual goal of inference and prediction, this extension may boost the model’s predictive power, depending on the dataset.

Because we orthogonalize the smooth component of our model with respect to  $\mathbf{z}_\theta(\mathbf{s}, x)$  at observed depths, let  $\mathbf{Z}(\mathbf{s}_{ij})$  be a matrix with  $\mathbf{z}_\theta(\mathbf{s}_{ij}, x)$  at all measured depths, and define the projection into the orthogonal columns space of  $\mathbf{Z}(\mathbf{s}_{ij})$  as

$$P_z^\perp(\mathbf{s}_{ij}) = \mathbf{I} - \mathbf{Z}(\mathbf{s}_{ij}) (\mathbf{Z}(\mathbf{s}_{ij})^T \mathbf{Z}(\mathbf{s}_{ij}))^{-1} \mathbf{Z}(\mathbf{s}_{ij})^T.$$

Note that we do not include a column of ones in  $\mathbf{Z}(\mathbf{s}_{ij})$  because we wish to preserve the simple correspondence between  $\alpha(\mathbf{s})$  and the expected snow density at the surface (i.e.,  $x = 0$ ).

If we let  $\mathbf{h}_\theta^\perp(\mathbf{s}_{ij}, x) = P_z^\perp(\mathbf{s}_{ij})\mathbf{h}(x)$ ,  $\mathbf{h}(x)$  are covariates specified through basis functions of smooth curves (e.g., polynomial splines), then the smoothed Arrhenius regression model is

$$\log \left( \frac{\mu(\mathbf{s}_{ij}, x)}{\rho_I - \mu(\mathbf{s}_{ij}, x)} \right) = \alpha(\mathbf{s}) + \mathbf{z}_\theta(\mathbf{s}_{ij}, x)^T \mathbf{k}(\mathbf{s}) + \mathbf{h}_\theta^\perp(\mathbf{s}_{ij}, x)^T \boldsymbol{\beta}(\mathbf{s}), \quad (6)$$

where  $\boldsymbol{\beta}(\mathbf{s})$  are spatially-varying mean-zero coefficients. We write this model in terms of  $\mu(\mathbf{s}_{ij})$  rather than  $\mu(\mathbf{s})$  because the projection is dependent on depths measured at core  $\mathbf{s}_{ij}$ .

The parameters, however, still only depend on location  $\mathbf{s}$ . This model preserves inference on Arrhenius parameters but is more flexible, allowing deviations from piecewise linearity. Of course,  $\mathbf{h}_\theta^\perp(\mathbf{s}_{ij}, x)^T \boldsymbol{\beta}(\mathbf{s})$  could be replaced with a mean-zero Gaussian random effect with covariance  $\mathbf{S}$  augmented as  $P_z^\perp(\mathbf{s}_{ij}) \mathbf{S} P_z^\perp(\mathbf{s}_{ij})^T$ . Given the relatively simple shape of these data and the number of measurements, we use polynomials and splines instead of Gaussian processes.

## 4 Methods and Models

### 4.1 Models Comparison

In our comparison, we address four modeling questions: (1) Which truncated error distribution best suits these data? (2) How should we account for group differences in measurement accuracy, including the core length used to obtain density measurements? (3) Which cross-covariance model is best for our spatially-varying Arrhenius regression model? (4) Should our model include deviations from the piece-wise linearity by including *smoother* components to the model?

We use the Watanabe–Akaike information criterion (WAIC) as our model selection criterion (Watanabe, 2010), computed using each observation as a partition (Vehtari et al., 2017). We use WAIC in favor of deviance information criterion (DIC) (Spiegelhalter et al., 2002) because WAIC is a generally more stable approximation to cross-validation than DIC, uses the entire posterior distribution, and is less prone to select overfit models.

We discuss model comparison results in detail in Appendix A. To summarize the results, we find that using a truncated  $t$ -distribution is better than corresponding truncated Normal models. Error distributions with hierarchically-specified scale parameters, weighted to account for the length of the core used to obtain density measurements, improve WAIC relative to homoscedastic models. We select a separable cross-covariance model for the spatially-varying Arrhenius parameters because it has the lowest WAIC, but we did not find significant differences in model performance for most cross-covariance models. Lastly, we compare seven possible smooth adjustments to the piecewise linear Arrhenius model and

select a quadratic spline with three knots to specify (6) because it has the lowest WAIC; however, several spline models perform comparably. We present our final model in Section 4.2.

## 4.2 Hierarchical Model

Using the quantities defined in Section 2, our hierarchical model is

$$\begin{aligned}
 y(\mathbf{s}_{ij}, x) &\sim t_\nu \left( \mu(\mathbf{s}_{ij}, x), \tau_{\mathbf{s}_{ij}}^2, 0, \infty \right) \\
 \log \left( \frac{\mu(\mathbf{s}_{ij}, x)}{\rho_I - \mu(\mathbf{s}_{ij}, x)} \right) &= \alpha(\mathbf{s}) + \mathbf{z}_\theta(\mathbf{s}, x)^T \mathbf{k}(\mathbf{s}) + \mathbf{h}_\theta^\perp(\mathbf{s}_{ij}, x)^T \boldsymbol{\beta}(\mathbf{s}) \\
 \log(\tau_{\mathbf{s}_{ij}}^2) &\sim \mathcal{N} \left\{ \log \left[ \tau_{m(\mathbf{s}_{ij})}^2 dx_{\mathbf{s}_{ij}}^{\eta_{m(\mathbf{s}_{ij})}} \right], \sigma_\tau^2 \right\},
 \end{aligned} \tag{7}$$

where  $t_\nu(\mu(\mathbf{s}_{ij}, x), \tau_{\mathbf{s}_{ij}}^2, 0, \infty)$  is a  $t$ -distribution with location  $\mu(\mathbf{s}_{ij}, x)$ , scale  $\tau_{\mathbf{s}_{ij}}$ , and truncated below by 0. We use the truncated- $t$  distribution to give a coherent model, but the truncation has no practical effect on our analysis because snow densities are not close to zero. For the EAP and SEAT campaigns, there is no variation in  $dx_{\mathbf{s}_{ij}}$ ; therefore, we fix  $\eta_{m(\mathbf{s}_{ij})} = 0$  because this weighting parameter is not identifiable.

We specify a joint spatial process for the Arrhenius regression model through a joint multivariate Gaussian process (MGP) model for prior distribution for the intercept, transformed Arrhenius parameters, and critical densities. We let  $\boldsymbol{\theta}(\mathbf{s})$  be transformed spatial parameters,  $\alpha(\mathbf{s})$ ,  $\log(A_1(\mathbf{s}))$ ,  $\log(A_2(\mathbf{s}))$ ,  $\log(A_3(\mathbf{s}))$ ,  $\log(A_4(\mathbf{s}))$ ,  $\log(E_1(\mathbf{s}))$ ,  $\log(E_2(\mathbf{s}))$ ,  $\log(E_3(\mathbf{s}))$ ,  $\log(E_4(\mathbf{s}))$ ,  $\log\left(\frac{\rho_1(\mathbf{s})-0.42}{0.68-\rho_1(\mathbf{s})}\right)$ ,  $\log\left(\frac{\rho_2(\mathbf{s})-0.68}{0.78-\rho_2(\mathbf{s})}\right)$ , and  $\log\left(\frac{\rho_3(\mathbf{s})-0.78}{0.88-\rho_3(\mathbf{s})}\right)$ . We specify  $\boldsymbol{\theta}(\mathbf{s})$  using a multivariate GP; thus, the transformed spatial parameters at observed sites  $\boldsymbol{\theta}(\mathcal{S}) = (\boldsymbol{\theta}(\mathbf{s}_1)^T, \dots, \boldsymbol{\theta}(\mathbf{s}_{n_s})^T)^T$  follows a multivariate-normal distribution. That is,

$$\boldsymbol{\theta}(\mathcal{S}) \sim \mathcal{N}(\mathbf{M}\boldsymbol{\gamma}, \mathbf{R} \otimes \mathbf{V}), \tag{8}$$

where the hierarchical mean for  $\boldsymbol{\theta}(\mathbf{s})$  is

$$\mathbf{M}\boldsymbol{\gamma} = (\gamma_\alpha, \gamma_{A_1}, \gamma_{A_2}, \gamma_{A_2}, \gamma_{A_2}, \gamma_{E_1}, \gamma_{E_2}, \gamma_{E_2}, \gamma_{E_2}, \gamma_{\rho_1}, \gamma_{\rho_2}, \gamma_{\rho_3})^T,$$

$\boldsymbol{\gamma} = (\gamma_\alpha, \gamma_{A_1}, \gamma_{A_2}, \gamma_{E_1}, \gamma_{E_2}, \gamma_{\rho_1}, \gamma_{\rho_2}, \gamma_{\rho_3})^T$ , and  $\mathbf{M}$  is a  $12 \times 8$  matrix that repeats elements of  $\boldsymbol{\gamma}$ . We use repeated elements in our hierarchical mean because densification rates show little or weak transitions at the second and third critical densities (Hörhold et al., 2011). The  $i$ th row and  $i'$ th column of the correlation matrix  $\mathbf{R}$  is  $\exp(\phi d(\mathbf{s}_i, \mathbf{s}_{i'}))$ .

For the spatial model for the regression coefficients  $\beta_m(\mathbf{s})$ , we assume

$$\beta_m(\mathcal{S}) \sim \mathcal{N}(0, \sigma_{\beta_m}^2 \mathbf{R}_\beta), \quad (9)$$

where the  $i$ th row and  $i'$ th column of the correlation matrix  $(\mathbf{R})_{i,i'} = \exp(-\phi_\beta d(\mathbf{s}_i, \mathbf{s}_{i'}))$ . Therefore, we assume that the spatially-varying spline coefficients are centered on zero, share a common decay parameter, but have their own scale parameter.

### 4.3 Prior Distributions, Model Fitting, and Prediction

We use the following prior distributions for our hierarchical model:

$$\begin{aligned} \gamma_\alpha &\sim \mathcal{N}(-0.5, 0.5^2) & \gamma_{\rho_1} &\sim \mathcal{N}(0, 1) & \sigma_\tau^2 &\sim \mathcal{IG}(2.1, 1/10) \\ \gamma_{A_1} &\sim \mathcal{N}(2.4, 0.2^2) & \gamma_{\rho_2} &\sim \mathcal{N}(0, 1) & \mathbf{V} &\sim \text{Inverse-Wishart}(13, \mathbf{I}) \\ \gamma_{A_2} &\sim \mathcal{N}(6.35, 0.2^2) & \gamma_{\rho_3} &\sim \mathcal{N}(0, 1) & \phi^{-1} &\sim \text{Unif}(10, 1000) \\ \gamma_{E_1} &\sim \mathcal{N}(9.23, 0.2^2) & \nu &\sim \text{Unif}(4, 30) & \sigma_{\beta_l}^2 &\sim \mathcal{IG}(2.1, 1/10) \\ \gamma_{E_2} &\sim \mathcal{N}(9.97, 0.25^2) & \log(\tau_{m(\mathbf{s}_{ij})}^2) &\sim \mathcal{N}(-7, 4) & \phi_\beta^{-1} &\sim \text{Unif}(10, 1000) \\ & & \eta_{m(\mathbf{s}_{ij})} &\sim \mathcal{N}(-8, 4) & & \end{aligned} \quad (10)$$

The hierarchical mean parameters are informative and based on proposed Arrhenius constant parameters in Herron & Langway (1980). Because the  $t$ -distribution appears nearly Gaussian  $\nu \geq 30$ , we set 30 degrees of freedom as the upper bound. We set the lower bound on  $\nu$  to be four so that the first four moments of the error distribution are finite. The prior median for  $\log(\tau_{m(\mathbf{s}_{ij})}^2)$  corresponds to a median standard deviation of about 0.03 (for large  $\nu$ ) but allows much larger and smaller values. We choose this because, for a fixed depth, observations are quite concentrated about the center of the density curve. Because we do not know how much values of  $\log(\tau_{\mathbf{s}_{ij}}^2)$  may vary, we use a somewhat diffuse prior distribution

on  $\sigma_\tau^2$ . We choose this prior distribution for  $\eta_{m(\mathbf{s}_{ij})}$  because using more of the core to obtain a density measurement yields a smoother curve (i.e., less variance).

We use uniform prior distributions for the range parameters of our spatially-varying piecewise Arrhenius model  $\phi^{-1}$  and cubic spline coefficients  $\phi_\beta^{-1}$ . For the exponential correlation function, our prior distribution bounds the effective range of our spatially-varying parameters between 30 and 3,000 km. Because we expect the spatially-varying parameters of our model not to differ much from the hierarchical means, we use flexible prior distributions for  $\mathbf{V}$  and  $\sigma_{\beta_l}^2$  that heavily weight small values. For exponential covariance models, only the product of scale and decay parameters is identifiable, and model-based interpolations are equal if the product of scale and decay parameters is equal (Zhang, 2004). Thus, we are not able to make good inference on  $\phi$ ,  $\phi_\beta$ ,  $\mathbf{V}$ , on  $\sigma_{\beta_l}^2$  individually.

We use an adaptive Markov chain Monte Carlo (MCMC) model fitting approach to obtain posterior samples using Metropolis-within-Gibbs and Gibbs updates. We sample Arrhenius regression parameters  $\theta(\mathbf{s})$  site-wise using the multivariate Metropolis algorithm with multivariate Normal proposal distributions centered on the current parameter values and covariance equal to the scaled empirical covariance of the site-specific parameters (Haario et al., 2001). We use the univariate Metropolis algorithm updates with Normal random walk proposal distributions to sample from the posterior distributions of  $\beta_l(\mathbf{s})$  and  $\nu$ , while we use the univariate Metropolis-Hastings algorithm with log-Normal random walk proposal distributions to sample from the posterior distributions of  $\tau^2(\mathbf{s}_{ij})$ ,  $\phi$ , and  $\phi_\beta$ . During the burn-in part of our MCMC, we tune the candidate variances so that acceptance rates are between 0.2-0.6 for univariate updates and 0.15-0.5 for multivariate updates. Because spatially-varying parameters mix slowly due to high correlation, we follow the recommendation of Neal (1998), updating the spatially-varying parameters several times, five, in this case, each iteration of the sampler. Because posterior conditional distributions for  $\gamma$ ,  $\log(\tau_{m(\mathbf{s}_{ij})}^2)$ ,  $\eta_{m(\mathbf{s}_{ij})}$ ,  $\sigma_\tau^2$ , and  $\sigma_{\beta_l}^2$  can be found in closed form, we update these parameters using Gibbs updates.

Using our model, we can estimate model parameters and mean density curves. Our primary goal is estimating how various parameters (or functions of parameters) vary spatially. To estimate Arrhenius parameters at new locations  $\mathbf{s}_{new}$ , we simply sample the transformed parameters  $\theta(\mathbf{s}_{new})$  using the appropriate conditional normal distribution. If estimating the

mean  $\mu(\mathbf{s}, x)$  or observed density  $y(\mathbf{s}, x)$  at a location outside of  $\mathcal{S}$ , then we follow the same process for interpolating regression spline coefficients as with Arrhenius coefficients and use composition sampling to sample from the posterior predictive distribution (Tanner, 1996).

## 5 Results

We run our MCMC model fitting for 250,000 iterations, discard the first 50,000, and keep every 20th sample. Our results are based on the remaining 10,000 posterior samples. Before presenting results, we again clarify that the truncated- $t$  distribution gives a coherent model, but the truncation has no practical effect on our analysis because snow densities are not close to zero. For this reason, we do not discuss this further.

### 5.1 Hierarchical Summaries

In this subsection, we present the posterior summaries of the hierarchical Arrhenius parameters and compare the hierarchical mean to the parameter estimates of the HL model, as well as other scientific assertions about firn densification (Revisit Section 2.1 for this discussion). We defer discussion of several parameters to Appendix B. We present posterior summaries (posterior mean, median, standard deviation, and a 90% central credible interval) in Table 1. To compare previous parameter estimates to our posterior distribution, we calculate the quantile of our posterior distribution corresponding to the previous estimates (See Table 1).

Arrhenius parameter estimates in the HL model correspond to quantiles between (0.365 and 0.756). The first critical density suggested by Herron & Langway (1980), 0.55 g/cm<sup>3</sup>, corresponds to the 84% of our posterior distribution, suggesting that the firn cores in our dataset suggest a lower critical density than that in Herron & Langway (1980). As discussed in Hörhold et al. (2011), several studies suggest critical densities at 0.73 and 0.83 g/cm<sup>3</sup>, which are, respectively, the 0.27 and 0.07 quantile of the posterior distribution. Although the hierarchical mean of our spatially-varying Arrhenius model is compatible with previous scientific estimates for firn densification, a global model for firn densification fails to accurately capture site-specific density patterns. We explore how these patterns change over space in Section 5.2.



In Figure 5, we give violin plots of the posterior distributions for the core-specific scale parameters  $\sqrt{\tau_{\mathbf{s}_{ij}}^2}$ . Recall that  $\log(\tau_{\mathbf{s}_{ij}}^2)$  are hierarchically-specified and factor in expedition-specific scale and weighting parameters to account for the length of the core used to obtain density measurements, as well as expedition differences. The differences between expeditions are apparent in Figure 5. EAP snowpits and SEAT cores generally have shorter averaging lengths  $dx_{\mathbf{s}_{ij}}$ ; thus, unsurprisingly, EAP snowpits have the highest estimated standard deviation, followed by SEAT cores. SDM and US cores have smaller estimated standard deviations, on average, but the US cores show high variability in standard deviation.

## 5.2 Spatially-Varying Parameters

In this section, we focus on the spatially-varying component of our model. Specifically, we interpolate all spatially-varying Arrhenius parameters on a grid of about 2500 points over the convex hull of our data. Importantly, our model’s Arrhenius constants depend on temperature 10-m below the surface. We rely on model-based spatial interpolations presented in Section 2 to estimate  $T(\mathbf{s})$  which, together with  $A_l(\mathbf{s})$ ,  $E_l(\mathbf{s})$ , define the Arrhenius constant for the  $l$ th stage of densification.

In Figure 6, we plot the posterior median of surface density, three critical densities, and the Arrhenius constants and parameters for the first two densification stages. We use the median because the untransformed parameters have some extreme values. In each plot, we plot the location of observations and note that the uncertainty in our estimates increases as the distance to observations increases. We estimate great heterogeneity in the spatially-varying parameters. We give measures of uncertainty for all spatially-varying parameters in Appendix B. From these uncertainty plots, we see the expected trends we would expect using a spatial model: uncertainty is higher (i) as the distance to observations increases and (ii) at the boundary of where our data is.

We follow-up on the assertion that stages two, three, and four are not significantly different (Hörhold et al., 2011) which we assume is true in the mean of the hierarchical model. To do this, we compute and plot the posterior probability that  $k_2(\mathbf{s}) > k_3(\mathbf{s})$ ,  $k_2(\mathbf{s}) > k_4(\mathbf{s})$ , and  $k_3(\mathbf{s}) > k_4(\mathbf{s})$  in Figure 7. In general, the estimated differences appear to be somewhat weak confirming the suggestion of Hörhold et al. (2011). However, there appear to be some

regional differences that contradict this assertion.

### 5.3 Comparison of Firn Density Estimates

To highlight the differences between the original HL model (2), the spatially-varying Arrhenius model (5), and the smoothed spatially-varying Arrhenius model (6), we revisit the cores discussed in Figure 3. For these four cores, we plot the three model fits in Figure 8. For all cores, there is a clear improvement using both of our proposed models. However, the smoothed Arrhenius regression model is only apparently better for some cores. For the two SDM cores, 4 and 8, there is no evident improvement using the more complicated smoothed Arrhenius regression model. For core 12, the smoothed Arrhenius regression model is much better than the piecewise Arrhenius model, while it is only slightly better for core 49. Overall, we find that the smoothed Arrhenius regression model was best for data-rich cores and provided only marginal improvement for cores with relatively fewer measurements.

## 6 Conclusions and Future Work

We analyzed a dataset of 14,844 density measurements taken from 57 firn cores drilled at 56 sites in West Antarctica using a novel spatially varying Arrhenius regression model. Our model allowed us to explore how important physical quantities vary over West Antarctica. Using this model, we explored how estimated firn densification patterns change over space and compared our model to previous studies.

This research opens several paths forward. Because acquiring in-situ snow density data is expensive, we plan to pursue a follow-up project proposing a spatial design method for selecting where and how deep cores should be drilled. As more data become available, we speculate that richer spatial models may be beneficial. More recently, firn cores are measured using high-resolution approaches that yield  $\approx 50,000$  density measurements per core. With such cores, smoothed Arrhenius regression models become computationally prohibitive; thus, we suggest exploring appropriate approximations for this framework. Future extensions could explore stochastic differential equation models for firn density.

This research opens several paths to further advance the state of polar cryospheric science.

Several areas of the discipline rely on spatially-distributed estimates of firn density with depth. The proposed density modeling framework should be immediately applicable to estimates of annual surface mass balance using radar data, which require firn density as input (Keeler et al., 2020). Additionally, recent investigations of Antarctica increasingly rely on the outputs of coupled climate models and climate reanalyses to investigate SMB, mass loss, and similar climate changes (Lenaerts et al., 2012; Wessem et al., 2018). The improved prediction of firn/ice densities from the results of this study can provide context for these climate models and help to assess their performance for regions across West Antarctica. Finally, due to the large commitment and expense required for *in-situ* data collection in Antarctica, the careful selection of ice/firn coring sites is essential for expedition planning and execution. We therefore plan to pursue a follow-up project proposing a spatial design method for selecting where and how deep cores should be drilled.

As more data become available, we speculate that richer spatial models may be beneficial. More recently, firn cores are measured using high-resolution approaches that yield  $\approx 50,000$  density measurements per core. With such cores, smoothed Arrhenius regression models become computationally prohibitive; thus, we suggest exploring appropriate approximations for this framework. Future extensions could explore stochastic differential equation models for firn density.

## References

- Albert, M., Shuman, C., Courville, Z., Bauer, R., Fahnestock, M., & Scambos, T. (2004). Extreme firn metamorphism: Impact of decades of vapor transport on near-surface firn at a low-accumulation glazed site on the East Antarctic plateau. *Annals of Glaciology*, 39, 73–78.
- Alley, R. B., Bolzan, J. F., & Whillans, I. M. (1982). Polar firn densification and grain growth. *Annals of Glaciology*, 3, 7–11.
- Álvarez, M. A., & Lawrence, N. D. (2011). Computationally efficient convolved multiple output Gaussian processes. *Journal of Machine Learning Research*, 12(May), 1459–1500.

- Arthern, R. J., Vaughan, D. G., Rankin, A. M., Mulvaney, R., & Thomas, E. R. (2010). In situ measurements of Antarctic snow compaction compared with predictions of models. *Journal of Geophysical Research: Earth Surface*, *115*(F3). Retrieved 2020-06-05, from <https://agupubs.onlinelibrary.wiley.com/doi/abs/10.1029/2009JF001306> (\_eprint: <https://agupubs.onlinelibrary.wiley.com/doi/pdf/10.1029/2009JF001306>) doi: 10.1029/2009JF001306
- Banerjee, S., Carlin, B. P., & Gelfand, A. E. (2014). *Hierarchical modeling and analysis for spatial data*. CRC press.
- Bohlander, J., & Scambos, T. (2001). Thermap Antarctic ice sheet temperature data. *Boulder, CO: National Snow and Ice Data Centre*.
- Burgener, L., Rupper, S., Koenig, L., Forster, R., Christensen, W. F., Williams, J., . . . Riley, L. (2013, May). An observed negative trend in West Antarctic accumulation rates from 1975 to 2010: Evidence from new observed and simulated records. *Journal of Geophysical Research-Atmospheres*, *118*(10), 4205–4216.
- Cuffey, K. M., & Paterson, W. S. B. (2010). *The physics of glaciers*. Academic Press.
- Eisen, O., Frezzotti, M., Genthon, C., Isaksson, E., Magand, O., van den Broeke, M. R., . . . Vaughan, D. G. (2008, April). Ground-based measurements of spatial and temporal variability of snow accumulation in East Antarctica. *Reviews of Geophysics*, *46*(1), RG2001. (WOS:000255079700001) doi: 10.1029/2006RG000218
- Freitag, J., Wilhelms, F., & Kipfstuhl, S. (2004). Microstructure-dependent densification of polar firn derived from x-ray microtomography. *Journal of Glaciology*, *50*(169), 243–250.
- Genton, M. G., & Kleiber, W. (2015). Cross-covariance functions for multivariate geostatistics. *Statistical Science*, 147–163.
- Gneiting, T., Kleiber, W., & Schlather, M. (2010). Matérn cross-covariance functions for multivariate random fields. *Journal of the American Statistical Association*, *105*(491), 1167–1177.

- Gow, A. J. (1975). Time-temperature dependence of sintering in perennial isothermal snowpacks. *International Association of Hydrological Sciences Publications*, 114, 25–41.
- Grzebyk, M., & Wackernagel, H. (1994). Multivariate analysis and spatial/temporal scales: real and complex models. In *Proceedings of the xviii international biometrics conference* (Vol. 1, pp. 19–33).
- Haario, H., Saksman, E., & Tamminen, J. (2001). An adaptive Metropolis algorithm. *Bernoulli*, 7(2), 223–242.
- Helsen, M. M., Broeke, M. R. v. d., Wal, R. S. W. v. d., Berg, W. J. v. d., Meijgaard, E. v., Davis, C. H., ... Goodwin, I. (2008, June). Elevation Changes in Antarctica Mainly Determined by Accumulation Variability. *Science*, 320(5883), 1626–1629. Retrieved 2020-06-05, from <https://science.sciencemag.org/content/320/5883/1626> (Publisher: American Association for the Advancement of Science Section: Report) doi: 10.1126/science.1153894
- Herron, M. M., & Langway, C. C. (1980). Firn densification: An empirical model. *Journal of Glaciology*, 25(93), 373–385.
- Hodges, J. S., & Reich, B. J. (2010). Adding spatially-correlated errors can mess up the fixed effect you love. *The American Statistician*, 64(4), 325–334.
- Hörhold, M. W., Kipfstuhl, S., Wilhelms, F., Freitag, J., & Frenzel, A. (2011). The densification of layered polar firn. *Journal of Geophysical Research: Earth Surface*, 116(F1).
- IPCC. (2013). *Climate Change 2013: The Physical Science Basis. Contribution of Working Group I to the Fifth Assessment Report of the Intergovernmental Panel on Climate Change*. Cambridge, United Kingdom and New York, NY, USA: Cambridge University Press.
- Johnson, J. B. (1998). A preliminary numerical investigation of the micromechanics of snow compaction. *Annals of Glaciology*, 26, 51–54.

- Keeler, D. G., Rupper, S. B., Forster, R., & Miège, C. (2020). A probabilistic automated isochrone picking routine to derive annual surface mass balance from radar echograms. *IEEE Transactions on Geoscience and Remote Sensing*, In Press.
- Kleiber, W., & Nychka, D. (2012). Nonstationary modeling for multivariate spatial processes. *Journal of Multivariate Analysis*, *112*, 76–91.
- Lamorey, G., & Cooper, T. (2002). *Siple dome waiscores density data for shallow cores*. Retrieved from <https://nsidc.org/data/waiscores/density.html>
- Lenaerts, J. T. M., van den Broeke, M. R., van de Berg, W. J., van Meijgaard, E., & Munneke, P. K. (2012, February). A new, high-resolution surface mass balance map of Antarctica (1979-2010) based on regional atmospheric climate modeling. *Geophysical Research Letters*, *39*, L04501. (WOS:000300794400004) doi: 10.1029/2011GL050713
- Li, J., & Zwally, H. J. (2011). Modeling of firn compaction for estimating ice-sheet mass change from observed ice-sheet elevation change. *Annals of Glaciology*, *52*(59), 1–7.
- Maeno, N., & Ebinuma, T. (1983). Pressure sintering of ice and its implication to the densification of snow at polar glaciers and ice sheets. *The Journal of Physical Chemistry*, *87*(21), 4103–4110.
- Martinerie, P., Raynaud, D., Etheridge, D. M., Barnola, J.-M., & Mazaudier, D. (1992). Physical and climatic parameters which influence the air content in polar ice. *Earth and Planetary Science Letters*, *112*(1-4), 1–13.
- Matheron, G. (1982). Pour une analyse krigeante des données régionalisées. *Centre de Géostatistique, Report N-732, Fontainebleau*.
- Mayewski, P. A., Frezzotti, M., Bertler, N., Ommen, T. V., Hamilton, G., Jacka, T. H., . . . Goodwin, I. (2005). The International Trans-Antarctic Scientific Expedition (ITASE): An overview. *Annals of Glaciology*, *41*, 180–185.
- Meyer, M. C. (2008). Inference using shape-restricted regression splines. *The Annals of Applied Statistics*, *2*(3), 1013–1033.

- Miège, C., Forster, R. R., Box, J. E., Burgess, E. W., McConnell, J. R., Pasteris, D. R., & Spikes, V. B. (2013). Southeast Greenland high accumulation rates derived from firn cores and ground-penetrating radar. *Annals of Glaciology*, *54*(63), 322–332.
- Molteni, F., Buizza, R., Palmer, T. N., & Petroliagis, T. (1996). The ECMWF ensemble prediction system: Methodology and validation. *Quarterly Journal of the Royal Meteorological Society*, *122*(529), 73–119.
- Neal, R. (1998). Regression and classification using Gaussian process priors. *Bayesian Statistics*, *6*, 475.
- Ramsay, J. O. (1988). Monotone regression splines in action. *Statistical Science*, *3*(4), 425–441.
- Salamatin, A. N., Lipenkov, V. Y., Barnola, J. M., Hori, A., Duval, P., & Hondoh, T. (2009). Snow/firn densification in polar ice sheets. *Low Temperature Science*, *68*(Supplement), 195–222.
- Spiegelhalter, D. J., Best, N. G., Carlin, B. P., & Van Der Linde, A. (2002). Bayesian measures of model complexity and fit. *Journal of the Royal Statistical Society: Series B (Statistical Methodology)*, *64*(4), 583–639.
- Tanner, M. A. (1996). *Tools for statistical inference* (3rd ed.). Springer-Verlag New York.
- Teh, Y. W., Seeger, M., & Jordan, M. I. (2005). Semiparametric latent factor models. *AISTATS 2005*, 333.
- Vehtari, A., Gelman, A., & Gabry, J. (2017). Practical Bayesian model evaluation using leave-one-out cross-validation and WAIC. *Statistics and computing*, *27*(5), 1413–1432.
- Verjans, V., Leeson, A. A., Nemeth, C., Stevens, C. M., Kuipers Munneke, P., Noël, B., & van Wessem, J. M. (2020). Bayesian calibration of firn densification models. *The Cryosphere Discussions*, *2020*, 1–23. Retrieved from <https://www.the-cryosphere-discuss.net/tc-2019-274/> doi: 10.5194/tc-2019-274

- Watanabe, S. (2010). Asymptotic equivalence of Bayes cross validation and widely applicable information criterion in singular learning theory. *Journal of Machine Learning Research*, *11*(Dec), 3571–3594.
- Wessem, J. M. v., Berg, W. J. v. d., Noël, B. P. Y., Meijgaard, E. v., Amory, C., Birnbaum, G., ... Broeke, M. R. v. d. (2018, April). Modelling the climate and surface mass balance of polar ice sheets using RACMO2 – Part 2: Antarctica (1979–2016). *The Cryosphere*, *12*(4), 1479–1498. Retrieved 2020-06-05, from <https://www.the-cryosphere.net/12/1479/2018/> (Publisher: Copernicus GmbH) doi: <https://doi.org/10.5194/tc-12-1479-2018>
- White, P. A., Keeler, D. G., & Rupper, S. (2020). Hierarchical spatial modeling of monotone west Antarctic snow density curves. *arXiv preprint arXiv:2001.05520*.
- White, P. A., Reese, C. S., Christensen, W. F., & Rupper, S. (2019). A model for Antarctic surface mass balance and ice core site selection. *Environmetrics*, *30*(8), e2579.
- Zhang, H. (2004). Inconsistent estimation and asymptotically equal interpolations in model-based geostatistics. *Journal of the American Statistical Association*, *99*(465), 250–261.

## A Model Comparison

Because the measurement are bounded below, we consider truncated Normal and truncated Student’s  $t$  error distributions for these data. To account for expedition differences, as well as the length of the core used to obtain each density measurement, we consider hierarchical and weighted models for the scale of the error distribution. Our model comparison question here is which components of this model are beneficial. For this comparison, we find that the truncated Student’s  $t$  distribution with weighted, hierarchical scale parameters has the lowest WAIC (See Table 2).

We consider eight possible cross-covariance specifications for the 12 spatially-varying parameters used to model these data that can be written in the form (see [Álvarez & Lawrence](#),



2011; Banerjee et al., 2014, for review):

$$\Sigma = (\Lambda \otimes \mathbf{I}) \text{BlockDiag}(\mathbf{R}_1, \dots, \mathbf{R}_r) (\Lambda^T \otimes \mathbf{I}). \quad (11)$$

In this model,  $\Lambda$  controls between-parameter dependence and is  $12 \times r$ , where  $r \leq 12$ . To govern spatial dependence, we use correlation matrices  $\mathbf{R}_1, \dots, \mathbf{R}_{12}$ , where the  $i$ th row and  $j$ th column of the  $k$ th correlation matrix is  $(\mathbf{R}_k)_{i,j} = \exp(\phi_k d(\mathbf{s}_{ij}, \mathbf{s}_l))$ . Here, we use  $d(\mathbf{s}_{ij}, \mathbf{s}_l)$  as the great-circle distance; however, other distance metrics may be just as effective in this application (e.g., the chordal distance). We consider the following possibilities:

**Independent:** If (a)  $\Lambda$  is  $12 \times 12$  identity matrix, then we assume no between-parameter dependence and  $\Sigma = \text{BlockDiag}(\mathbf{R}_1, \dots, \mathbf{R}_{12})$ .

**Separable:** If we let  $r = 12$  and  $\mathbf{R} = \mathbf{R}_1 = \mathbf{R}_2 = \dots = \mathbf{R}_{12}$ , then we get a separable model  $\Sigma = (\Lambda \Lambda^T) \otimes \mathbf{R}$ . This model is often called the intrinsic model of coregionalization (see Matheron, 1982). In this model, we assume that the spatial patterns for all parameters is similar and can be represented using a single correlation function .

**Latent Factor/Coregionalization:** If  $r < 12$ , then we get latent factor model and we cannot simplify (11). For a nice discussion of these models, see Teh et al. (2005). This model assumes that the we can describe the 12-dimensional spatial process using a lower-rank space. If we let  $r = 12$  and let  $\Lambda$  be lower-triangular, then we get the linear model of coregionalization and we cannot simplify (11) (see Grzebyk & Wackernagel, 1994, for early reference). In this model, we do not assume any rank-reduction.

Richer cross-covariance functions (see, e.g., Gneiting et al., 2010; Genton & Kleiber, 2015) or non-stationary cross-covariance functions (see, e.g., Kleiber & Nychka, 2012) are often beneficial. However, with  $n_s = 56$  sites, we have limited ability to estimate complicated spatial models and find that more complicated spatial models perform worse for this data. Moreover, many models have limited parameter identifiability; therefore, we argue that these cross-covariance functions offer sufficient flexibility.

Because the piecewise Arrhenius model (5) (the extended HL-model) is piecewise linear, we explore various specification of the smoothed Arrhenius model (6) to see whether they

improve upon (5). Specifically, we use a cubic polynomial, quadratic splines (with one, two, or three knots), and cubic splines (with one, two, or three knots). The results of the model comparison are given in Table 4. We use the cubic spline with two knots because it has the lowest WAIC; however, all spline models with two or more knots are comparable in terms of WAIC.

## B Extended Posterior Analysis

In Figure 9, we plot the mean empirical between-parameter correlation taken from the 56 sites. We examine the correlation on the transformed parameter scale to decrease the effects of large values. There are many strong correlations. We note only a few. The intercept and critical densities are all positively correlated. Interestingly, the log-transformed pre-exponentiation factors for the first and fourth stages have strong negative correlation with the critical densities.

We give violin plots for site-specific posterior distribution in Figures 10, 11, and 12. From these plots, we see three clear and unsurprising patterns: (1) Arrhenius parameters that govern densities at shallower depths have lower posterior variance compared to parameters for deeper densification stages. (2) Cores with more observations have better resolved posterior distributions. (3) Cores distant from other cores have higher variance.

In Figure 13, we plot the interquartile range of each spatially-varying parameter over the convex hull of our dataset. We use the interquartile range because untransformed parameters have extreme values. In general, uncertainty is highest near boundaries of our interpolation region and far from drilled cores.

Estimate Description	Function of Parameters	Previous Estimate Posterior Quantile	Mean	Median	Std. dev.	5%	95%
Surface Density	$\frac{\rho_I \exp(\gamma_\alpha)}{1 + \exp(\gamma_\alpha)}$	—	0.365	0.364	0.046	0.291	0.442
1st-stage $A$	$\exp(\gamma_{A_1})$	0.577	10.810	10.650	1.892	7.978	14.150
1st-stage $E$	$\exp(\gamma_{E_1})$	0.756	9.46e3	9.38e3	1.07e3	7.78e3	1.13e4
2nd-stage $A$	$\exp(\gamma_{A_2})$	0.511	578.700	572.800	80.540	457.900	719.700
2nd-stage $E$	$\exp(\gamma_{E_2})$	0.505	2.14e4	2.14e4	1.47e3	1.91e4	2.39e4
1st Critical Density	$f_1(\rho_1)$	0.835	0.524	0.522	0.026	0.484	0.571
2nd Critical Density	$f_2(\rho_2)$	0.267	0.739	0.741	0.014	0.714	0.760
3rd Critical Density	$f_3(\rho_3)$	0.071	0.846	0.847	0.010	0.828	0.860

Table 1: Posterior summaries of untransformed hierarchical Arrhenius parameters.

Truncated					
Distribution	Weighting	Hierarchical	WAIC	Relative WAIC	WAIC SE
Normal	Yes	Yes	-73234.89	3410.35	338.17
Student's- <i>t</i>	No	No	-73740.73	2904.52	272.37
Student's- <i>t</i>	Yes	No	-75297.33	1347.91	275.06
Student's- <i>t</i>	No	Yes	-75775.72	869.53	272.71
<b>Student's-<i>t</i></b>	<b>Yes</b>	<b>Yes</b>	<b>-75791.80</b>	<b>853.44</b>	<b>272.33</b>

Table 2: WAIC for models differing in their error distribution.

Cross-Covariance Function	WAIC	Relative WAIC	WAIC SE
<b>Separable GP</b>	<b>-75791.80</b>	<b>853.44</b>	<b>272.33</b>
Independent GP	-75766.30	853.44	272.82
2 Latent Factors	-74572.49	2072.76	267.38
4 Latent Factors	-75654.19	991.06	268.43
6 Latent Factors	-75600.94	1044.31	270.75
8 Latent Factors	-75606.62	1038.62	270.62
10 Latent Factors	-75776.52	868.72	271.53
Coregionalization (12 Latent Factors)	-75690.65	954.59	270.70

Table 3: WAIC for models differing by the cross-covariance of the transformed Arrhenius parameters.

Model for $\mathbf{h}_\theta^\perp(\mathbf{s}_{ij}, x)$	Number of Knots	WAIC	Relative WAIC	WAIC SE
None	—	-75791.80	853.44	272.33
Cubic Polynomial	—	-75822.69	822.56	272.95
Quadratic Spline	1	-76383.12	262.13	278.51
<b>Quadratic Spline</b>	<b>2</b>	<b>-76645.25</b>	<b>0.00</b>	<b>278.69</b>
Quadratic Spline	3	-76601.84	43.41	279.04
Cubic Spline	1	-76541.38	103.87	278.77
Cubic Spline	2	-76625.65	19.60	280.73
Cubic Spline	3	-76617.85	27.40	280.09

Table 4: WAIC for models differing by the smooth nonlinear adjustment to the piecewise linear model.

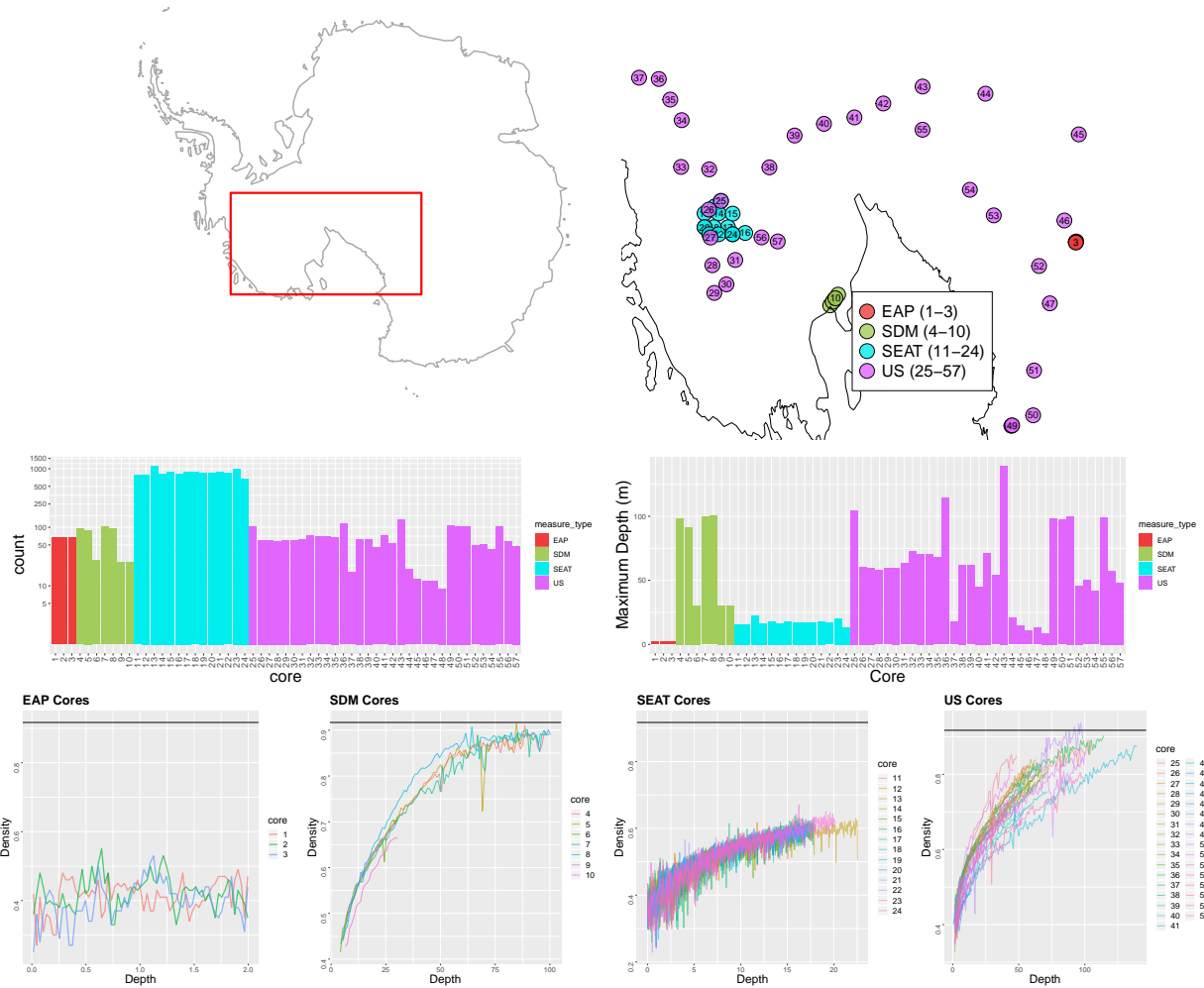


Figure 1: (Top-Left) Region of Antarctica where firn/ice cores are located. (Top-Right) Location of core sites with colors indicating measurement type. (Middle-Left) The number of density measurements at each core, and (Middle-Right) Maximum depth in m obtained by each core. (Bottom) Density measurements over depth by core, grouped by expedition. Note that the depth scales of these measurement types differ greatly. The horizontal line indicates the density of solid ice.

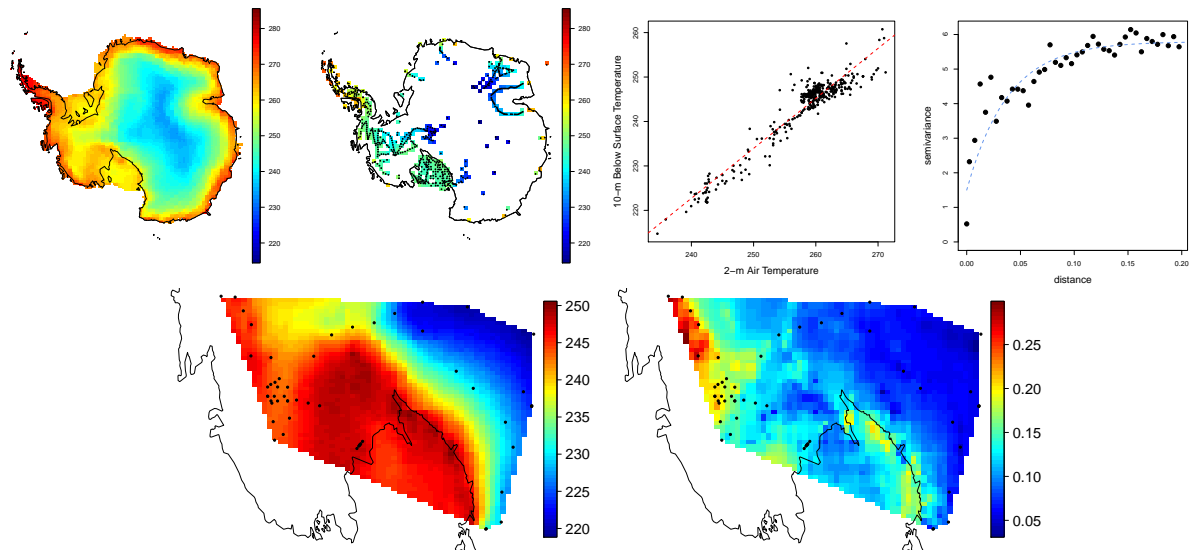


Figure 2: (Top-Left) Smoothed ERA-Interim 2-m air temperature averaged from 1979-2014. (Top-Center-Left) Temperature data 10-m below the surface. (Top-Center-Right) Relationship between nearest 2-m air temperature to observed temperature data 10-m below the surface. (Top-Right) Semivariogram for the residuals for temperature 10-m below the surface with a fit to an exponential semivariogram. (Bottom-Left) Temp-10 below (Bottom-Right) SMB

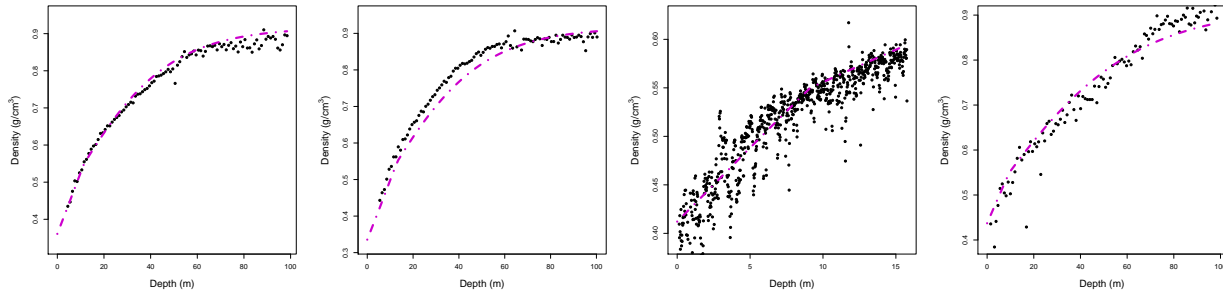


Figure 3: HL model fit to core (Left) 4, (Middle Left) 8, (Middle Right) 12, (Right) 49.

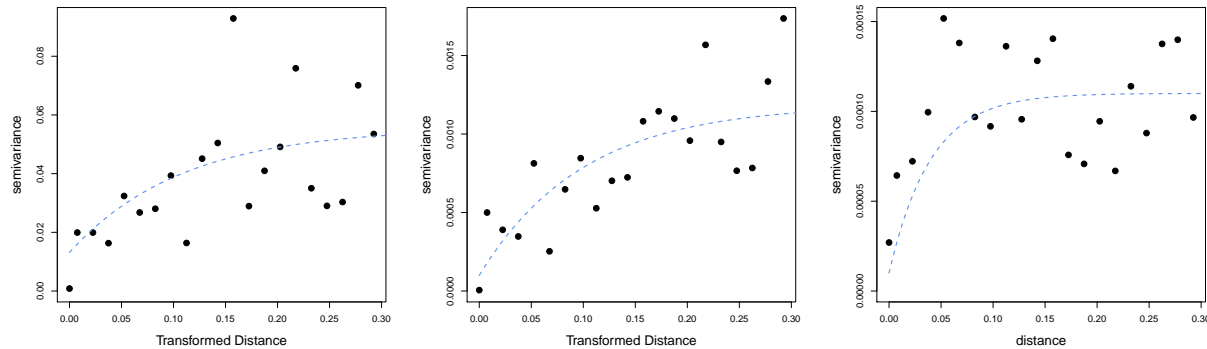


Figure 4: Empirical binned semivariogram for site-specific (Left) intercepts, (Center) First-stage Arrhenius constant, and (Right) Second-stage Arrhenius constants of the HL model. All binned semivariograms are plotted with a fit to an exponential semivariogram.



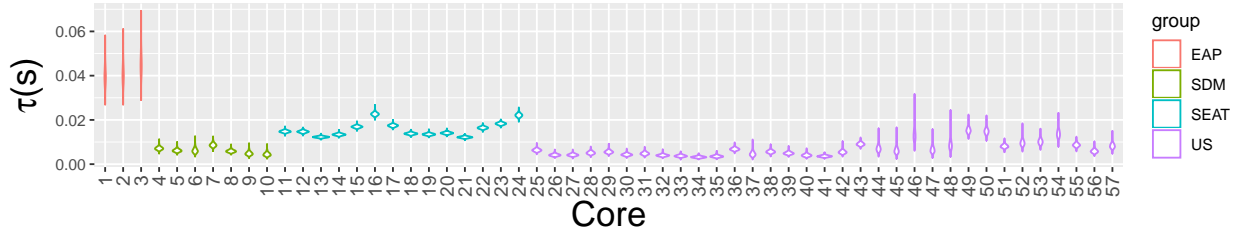


Figure 5: Posterior distributions for core-specific scale parameters.

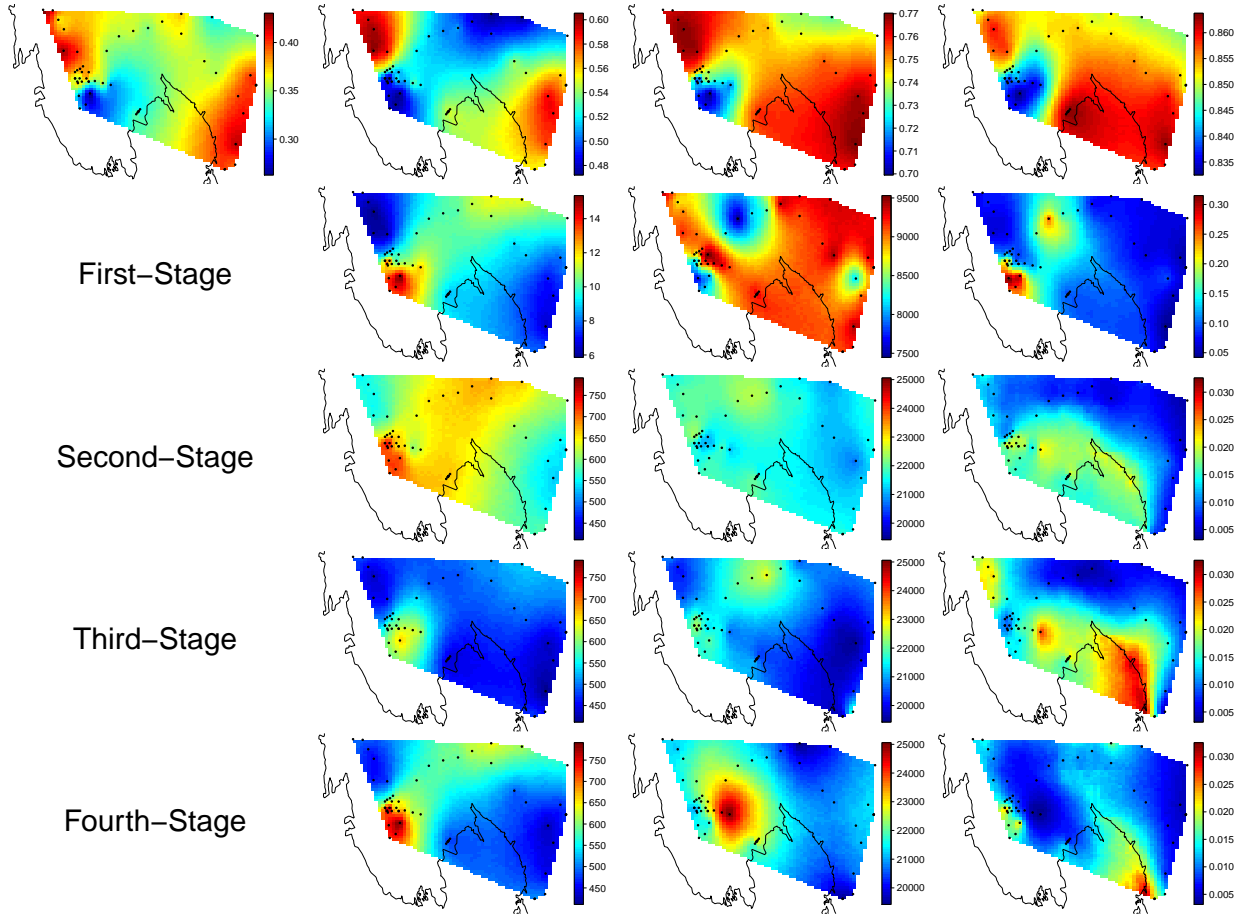


Figure 6: (Row 1) Posterior median for surface density and the three critical densities, all in  $\text{g}/\text{cm}^3$ , from left to right. (Rows 2-5) Posterior medians for  $A_l(\mathbf{s})$ ,  $E_l(\mathbf{s})$ , and  $k_l(\mathbf{s}) = A_l(\mathbf{s}) \exp\left(-\frac{E_l(\mathbf{s})}{RT(\mathbf{s})}\right)$ , for stages  $l = 1, 2, 3, 4$ . Second, third, and fourth stages share the same scale to allow visual comparison.

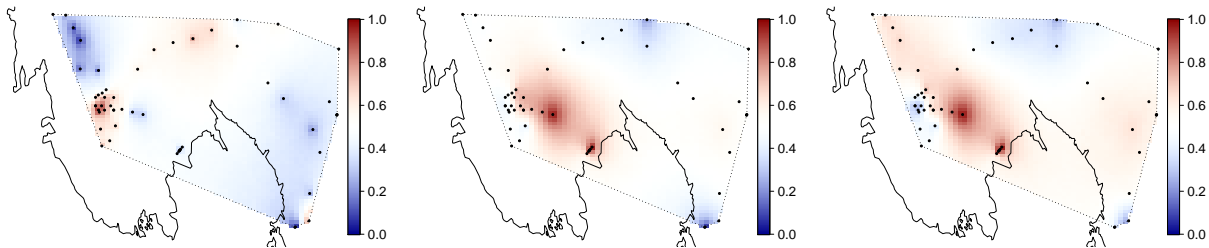


Figure 7: Posterior probability of (Left)  $k_2(\mathbf{s}) > k_3(\mathbf{s})$ , (Center)  $k_2(\mathbf{s}) > k_4(\mathbf{s})$ , and (Right)  $k_3(\mathbf{s}) > k_4(\mathbf{s})$ . Both small and large probabilities indicate differences between adjacent stages. The dotted line is the convex hull of our data.

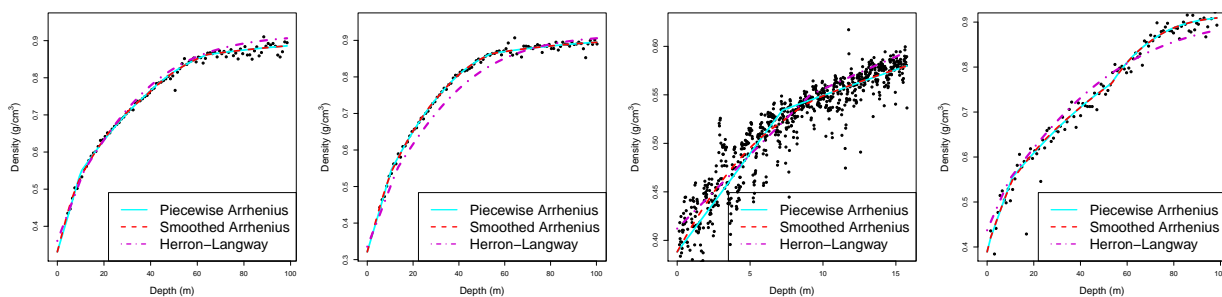


Figure 8: A comparison of the HL model, piecewise Arrhenius model, and the smoothed Arrhenius model for cores 4, 8, 12, and 49, from left to right. For the piecewise Arrhenius model and the smoothed Arrhenius model, we illustrate the model fit using the posterior mean.

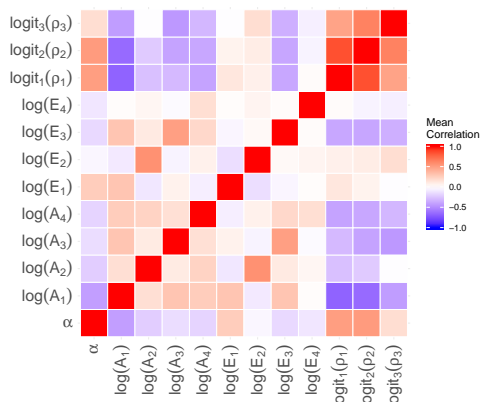


Figure 9: Empirical average between-parameter correlation estimated from 56 site-specific parameters.

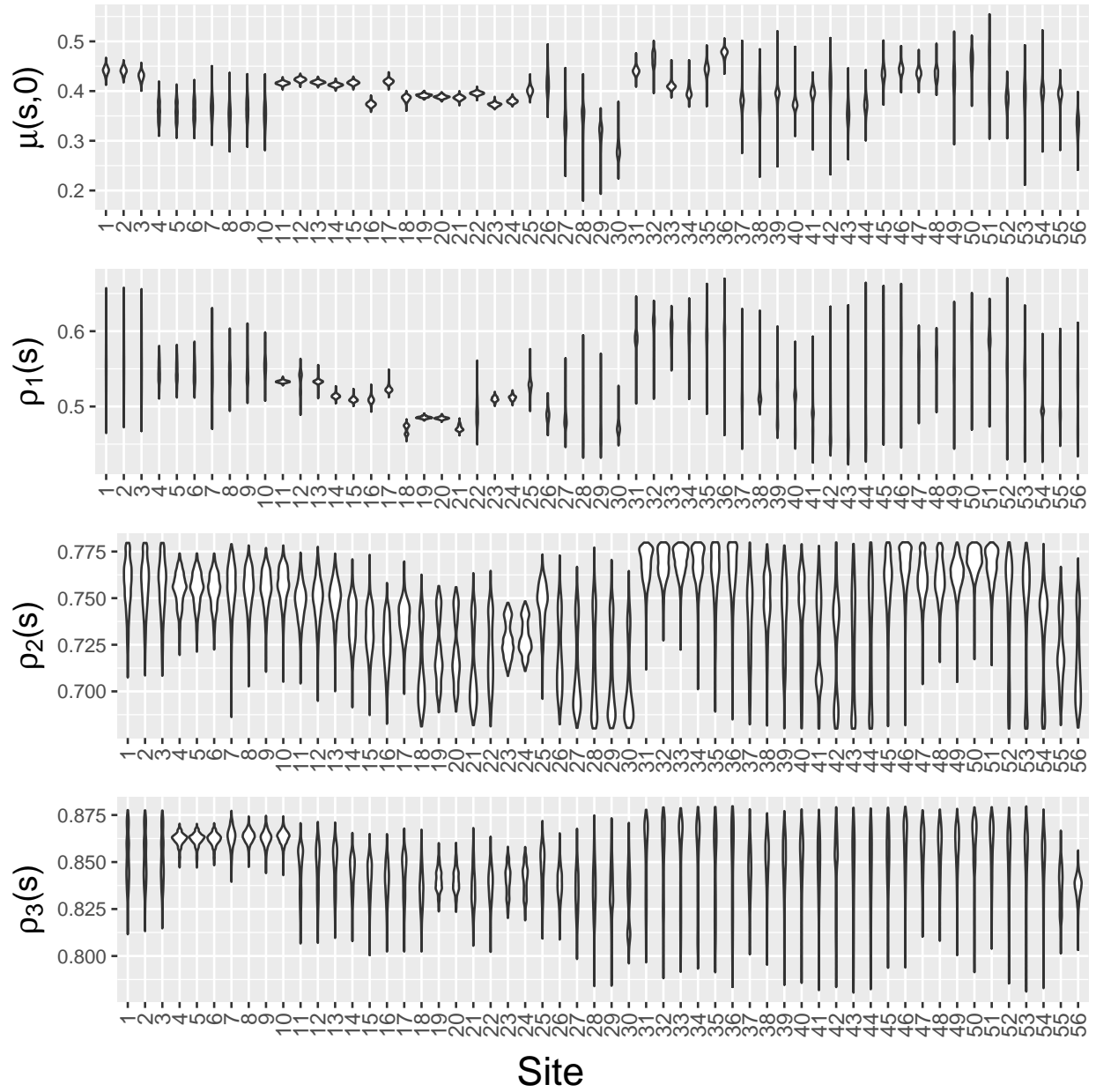


Figure 10: Posterior distributions for site-specific intercepts and critical densities.

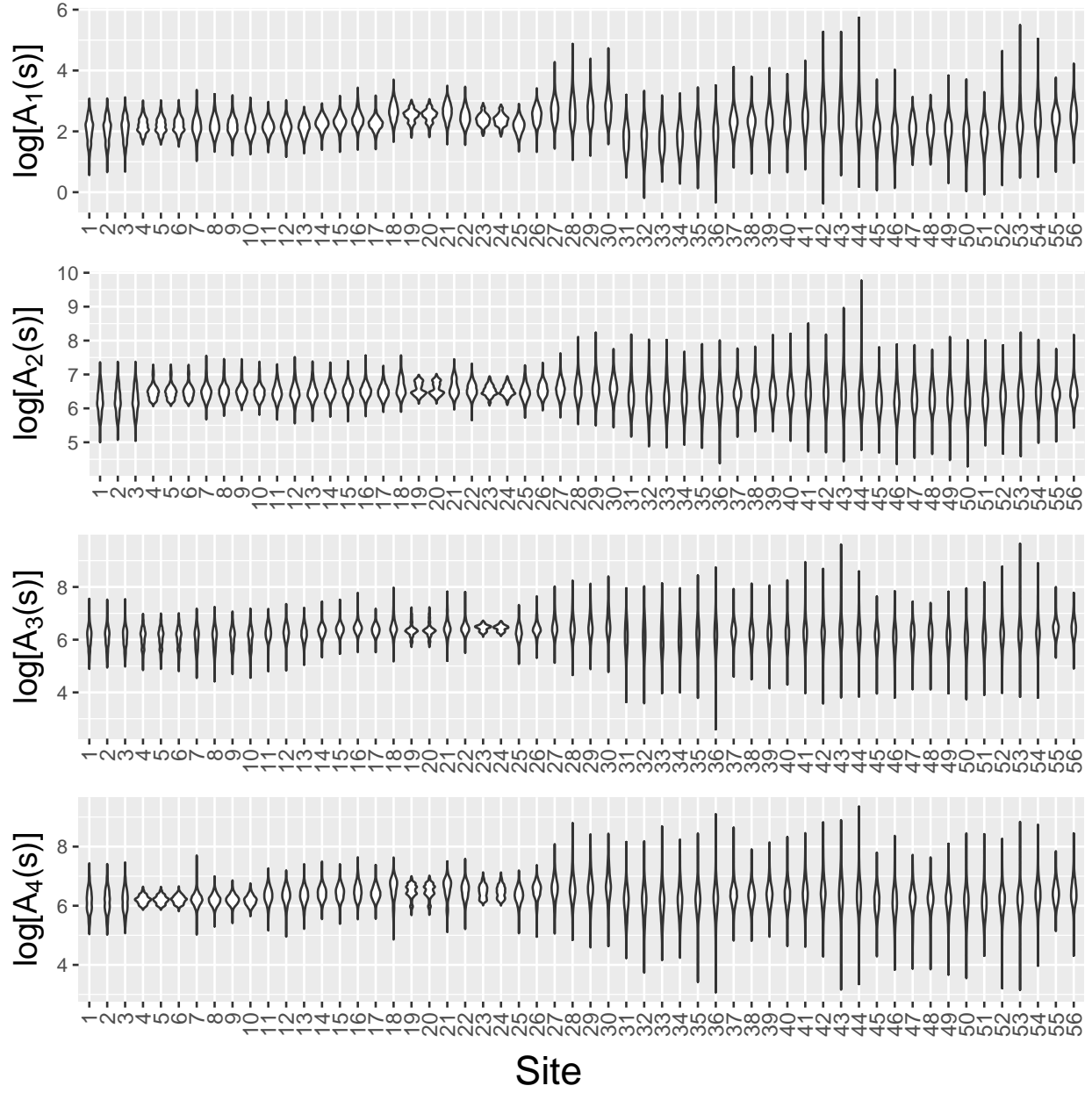


Figure 11: Posterior distributions for site-specific log-transformed pre-exponentiation factors.

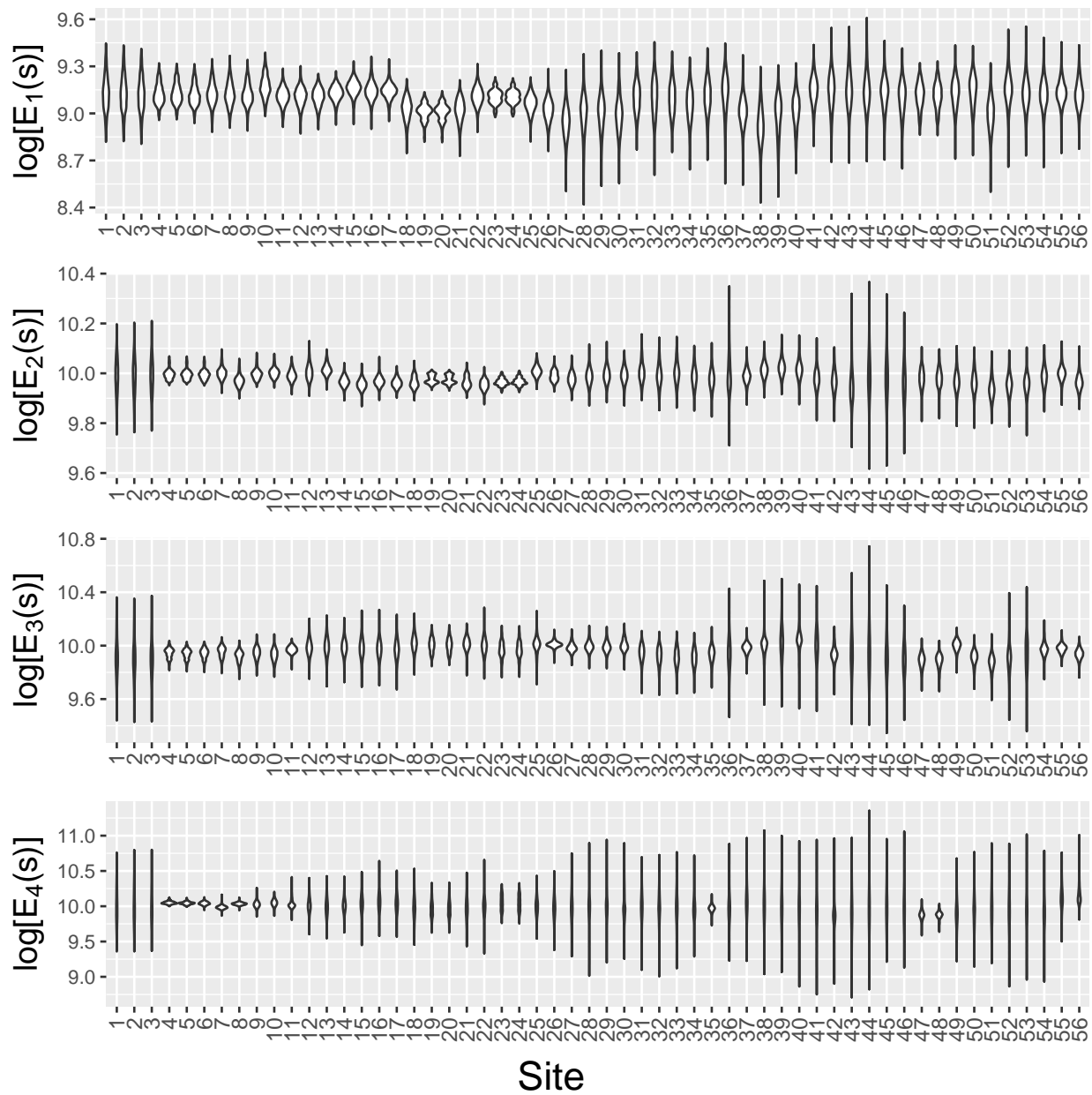


Figure 12: Posterior distributions for site-specific log-transformed energies of activation.

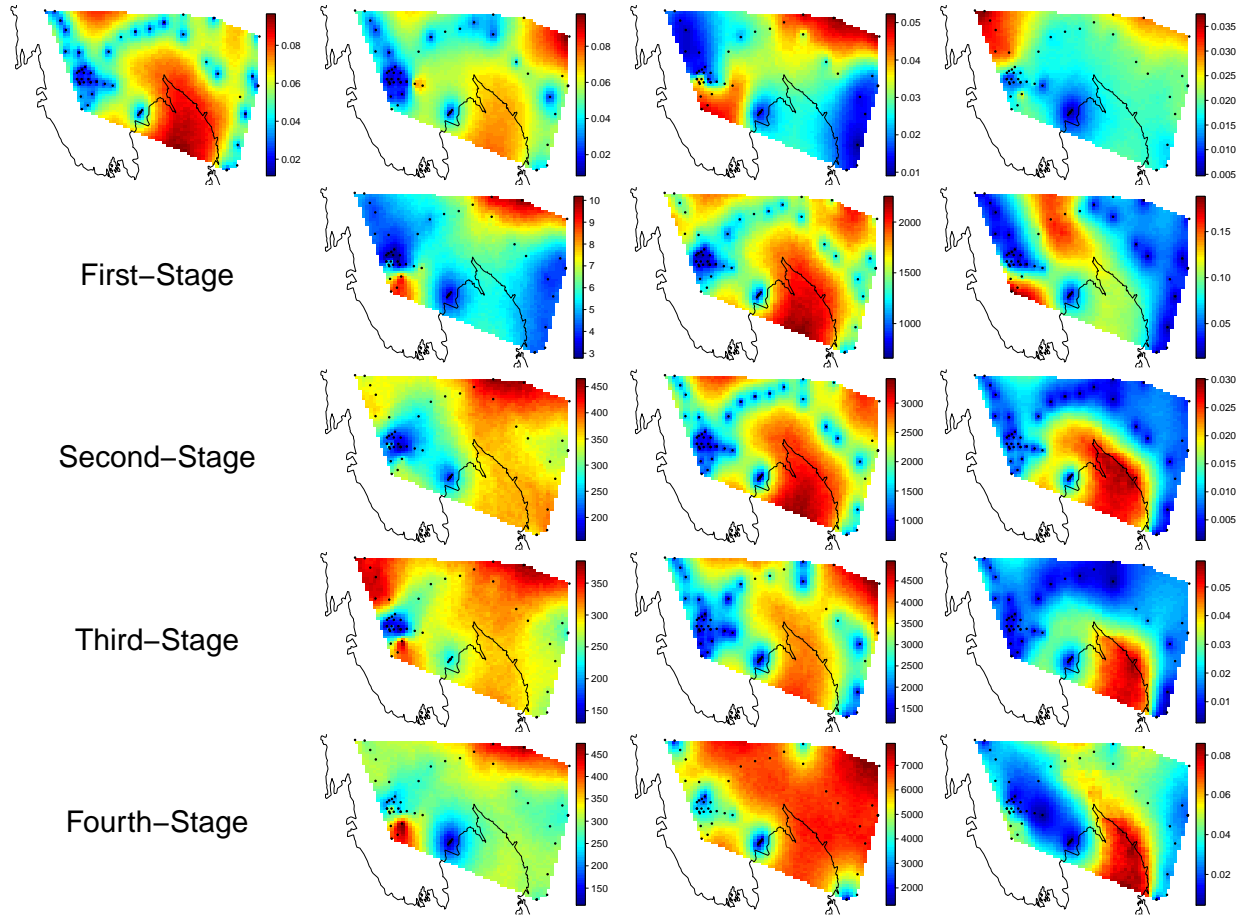


Figure 13: Interquartile range for (Row 1) surface density and the three critical densities, all in  $\text{g}/\text{cm}^3$ , from left to right. Interquartile range for (Rows 2-5)  $A_l(\mathbf{s})$ ,  $E_l(\mathbf{s})$ , and  $k_l(\mathbf{s}) = A_l(\mathbf{s}) \exp\left(-\frac{E_l(\mathbf{s})}{RT(\mathbf{s})}\right)$ , for stages  $l = 1, 2, 3, 4$ .